Near-Field Microwave Imaging of Biologically-Based Materials Using a Monopole Transceiver System

Paul M. Meaney, *Student Member, IEEE,* Keith D. Paulsen, *Member, IEEE,* and John T. Chang

***Abstract*—A prototype monopole-transceiver microwave imaging system has been implemented, and initial single and multitarget imaging experiments involving biologically relevant property distributions have been conducted to evaluate its performance relative to a previously developed waveguide system. A new, simplified, but more effective calibration procedure has also been devised and tested. Results show that the calibration procedure leads to improvements which are independent of the type of radiator used. Specifically, data–model match is found to increase by 0.4 dB in magnitude and 4° in phase for the monopoles and by 0.6 dB in magnitude and 7° in phase for the waveguides (on average) on a per measurement basis when the new calibration procedure is employed. Enhancements are also found in the reconstructed images obtained with the monopole system relative to waveguides. Improvements are observed in: 1) the recovered object shape; 2) the uniformity of the background; 3) edge detection; and 4) target property value recovery. Analyses of reconstructed images also suggest that there is a systematic decrease of approximately 10% in the reconstruction errors for the monopole system over its waveguide counterpart in single-target experiments and as much as a 20% decrease in multitarget cases. Results indicate that these enhancements stem from a better data–model match for the monopoles relative to waveguides which is consistent across the type of calibration procedure used. Comparisons of computations and measurements show an average improvement in data–model match of approximately 0.25 dB in magnitude and near 7° in phase in favor of the monopoles in this regard. Beyond this apparent imaging performance enhancement, the monopole system offers economy-of-space and low construction-cost considerations along with computational advantages (as described herein) which make it a compelling choice as a radiator/receiver element around which to construct a clinically viable near-field microwave imaging system.**

I. Introduction

WHILE active microwave imaging has been hypothesized as a potentially powerful medical-imaging modality for a number of years [1]–[3], there has yet to be any significant demonstration or realization of a clinically viable imaging system. As a result, the hypothesized clinical potential of this approach has remained unsubstantiated. There are two major difficulties which have retarded the development of active microwave imaging in the medical context. The first is the fact that image reconstruction cannot realistically proceed in terms of the classical projection-type algorithms which have dominated tomographic medical imaging. The second is the fact that data acquisition is difficult due to the significant tissue attenuation of the signals to be recorded and the potential for measurement artifacts arising from unwanted scattered fields and cross coupling between the transmit and receive elements within an imaging array.

A fair amount of attention has been paid to the reconstruction algorithm problem in recent years. The inadequacy and ultimate failure of diffraction-limit approximations [4] as the basis for microwave image reconstruction has motivated the development of near-field algorithms which properly account for the full-wave electromagnetic interactions in tissues. A variety of methods have been proposed [5]–[10] in this context and simulation studies indicate that these techniques provide a strong conceptual foundation upon which to pursue medical microwave imaging in practice. Unfortunately, these reconstruction methods are not without drawbacks. They are computationally intensive, with costs escalating significantly with increasing frequency. They have been studied primarily in theory and have not been used extensively in a laboratory setting. They require information from complex data-acquisition hardware that demands well-designed components and calibration procedures. Assuming that issues of computational costs will diminish over time, there remains a significant need to evaluate near-field algorithms with data measured from laboratory apparatus and to identify data-acquisition configurations which may be viable in a clinical setting.

On the hardware side of the problem, several prototype systems have been reported in the literature [11]–[14]. When coupled to diffraction-limited image-reconstruction methods these systems have been designed to operate in the low-gigahertz range (1–3 GHz) in order to achieve centimeter-scale spatial resolution [15]. The images obtained during laboratory experimentation have demonstrated that potentially useful qualitative information can be obtained [12], but that the overall approach is limited by the image reconstruction method [4], and that the tissue depths through which measurable microwave signals can be propagated are small relative to clinical interests. More recently, Meaney *et al.* [13], [16], [17] have demonstrated what appear to be the first laboratory-based confirmations of the viability of near-field image reconstruction of biologically relevant targets using frequencies as low

Manuscript received July 31, 1996; revised October 9, 1997. This work was supported by the National Institutes of Health under Grant RO1-CA55034.

P. M. Meaney and J. T. Chang are with the Thayer School of Engineering, Dartmouth College, Hanover, NH 03755 USA.

K. D. Paulsen is with the Thayer School of Engineering, Dartmouth College, Hanover, NH 03755 USA, and with the Norris Cotton Cancer Center, Dartmouth–Hitchcock Medical Center, Lebanon, NH 03755 USA.

Publisher Item Identifier S 0018-9480(98)00631-0.

as 300 MHz. This work also shows that in contrast to earlier diffraction-limited efforts, where only qualitative information was contained in the recovered images, quantitative reconstruction of the location, size, shape, and electrical properties (both real and imaginary components) of embedded objects can be obtained using near-field techniques [16].

Interestingly, in these previous hardware realizations of the data-acquisition system, waveguide-type radiators have been used exclusively as transmitters, and either waveguide [12], [14] or monopole/dipole [11], [13], [16] antennas have been used as receivers. The exclusive use of waveguide transmitters is not surprising because of the need to increase directivity and gain resulting from the requirement of placing the imaging region in the far-field—a restriction imposed by the diffraction-limited reconstruction algorithms that have been in use. The advent of near-field imaging strategies has eliminated this restriction in theory, which opens the door to considering other types of transmitting configurations. However, it is not immediately apparent whether other types of transmitting configurations, in particular, a monopole transmitter, would work effectively in practice. For example, the isotropic radiation pattern of a monopole can significantly reduce the size of the received signals and thereby compromise image quality because of decreased signal-to-noise ratio (SNR) being one of the critical determinants of near-field imaging performance. On the other hand, the monopole can be placed closer to the target region itself, and still illuminate the entire area of interest, whereas the directive antenna (i.e., waveguide) would need to be somewhat farther away (independent of near versus far-field considerations) in order for its main lobe to provide adequate illumination coverage. Clearly, either transmitter could be incorporated into an array design; however, if monopoles could be shown to be a viable transmitter, they offer an economy-of-space advantage that could become important as the number of independent transmit/receive channels increases. Further, since the experience with near-field image reconstruction using data collected with laboratory prototype microwave imaging systems is very recent and not extensive, there is intrinsic interest in evaluating different types of transmit and/or receive elements within this context.

Toward this end, we report our initial experience with near-field image reconstruction from laboratory data acquired with a monopole transceiver system. We demonstrate that such a radiator can be easily incorporated into our reconstruction algorithm and, in fact, leads to important computational economizations over our previous waveguide approach. Further, we illustrate a new and improved calibration procedure which directly addresses the sources of measurement error associated with antenna positioning discussed in [13], and which is independent of the type of radiating element used. The new calibration approach leads to images that are superior to those previously reported for waveguides as well as for monopoles as documented in the work contained herein. Most striking in this regard is the accurate reconstruction of the imaginary component of the electrical property distribution of small targets which were poorly recovered during earlier experiments [13]. We also find a systematic improvement in the monopole images relative to their waveguide counterparts which is attributed to better data–model match when the monopoles are employed.

The importance of these findings centers on the fact that they demonstrate that the more isotropic radiation pattern of the monopole does not serve to degrade imaging performance in the near-field context. The results also extend the robustness of the near-field approach by establishing a methodological independence on the type of radiator used. They contribute to the growing knowledge base on near-field image reconstruction from laboratory data by showing the capability of recovering quantitative images from monopole radiate/receive components which adds further support to the claim that near-field imaging is a viable path toward practical microwave imaging in a clinical context. It is important to note that the image reconstruction experiments performed herein have utilized mechanical repositioning of a single transmit and/or receive element in order to generate the multiple observations used during image reconstruction. Issues surrounding cross coupling between elements have not been addressed in this paper, but remain an important consideration under assumptions that one would utilize a fixed-array design for clinical data acquisition.

II. The Monopole Imaging System

Previous works by Meaney *et al.* [13], [16], [17] and Paulsen *et al.* [18] have demonstrated the initial capabilities of a prototype microwave imaging system which utilizes water-filled waveguides as radiators and an array of monopole antennas on the opposite side of the target region as detectors, all of which are suspended in a saline bath where TM illumination of various phantoms takes place. The configuration explored herein utilizes the same monopole antennas as both the transmit and receive elements. The monopoles were constructed by simply exposing a quarter-wavelength (in the medium at 500 MHz) of the center conductor (physical length was 2.5 cm) of a semirigid coaxial cable. While this type of antenna design is notorious for exciting currents along the outside of the coaxial cable in a low-loss medium such as air or deionized water, we have capitalized on the high attenuation of the surrounding saline solution to limit this effect. Details of the monopole performance in a lossy medium are reported [13], [17] where we have found its return loss in saline to be quite smooth over the broad bandwidth (300–1100 MHz) of interest. Information on the design, performance, and characteristics of the waveguide elements can also be found in [13] and [17].

The monopole transceiver arrangement presents the physical advantage of eliminating the more bulky waveguides in favor of a single type of simple antenna component which is conducive to a fixed-array data-acquisition design that may become important in realizing a clinically viable system. However, a number of operational issues surround the use of a monopole radiate–receive design within the context of near-field imaging and the performance of such a system vis-à-vis the previous waveguide approach needs to be investigated. In particular, we need to establish the level of data–model match which can be achieved with the computational solutions which

form the basis for image reconstruction with the monopole system and determine the extent to which the isotropic radiation pattern of the monopole element influences reconstructed image quality. In this section, we describe the operational aspects of the problems that were addressed in order to study a prototype monopole transceiver system.

A. Modified Reconstruction Algorithm

In terms of implementation within our reconstruction algorithm, the flexibility of the hybrid element (HE) strategy which we employ [9] lends itself nicely to the incorporation of the monopole radiator. Specifically, the monopole antennas can be treated as line sources within the homogeneous region modeled by the boundary element (BE) portion of the numerical model (i.e., the area outside the imaging region of interest), whereas the waveguide antennas required discretization as part of the BE method boundary, thus increasing the overall computational problem size. This change affects two aspects of the Newton–Raphson-based iterative image-reconstruction scheme: first, it requires modification of the forward solution (computation of the electric fields given the estimated electrical property distribution) which is calculated at each iteration and, second, it implies that modifications must be made to the Jacobian matrix calculation which is employed in computing the electrical property updates.

The required forward-solution modifications impact only the BE part of the numerical algorithm which is then coupled to the existing finite element (FE) discretization yielding a new complete HE representation. The radiating elements still reside within the homogeneous BE region except that the source has been changed from an equivalent field model involving Type I (Dirichlet) boundary conditions along the path of integration around each waveguide to that of a line source within the BE region represented by an inhomogeneous forcing term f in the governing Helmholtz equation

$$\nabla^2 E + k^2 E = -f, \qquad \text{where} \quad f = A\delta(x_s, y_s) \tag{1}$$

where

A	amplitude of the line source;
δ	Dirac delta function;
(x_s, y_s)	location of the radiator;
k^2	complex-valued wavenumber;
E	z-component of the electric field perpendicular to the imaging plane.

In matrix form (similar to that described in [19]), the new set of equations describing the electric-field distribution exterior to the electrically heterogeneous imaging region becomes

$$[D_{bb}]\{\boldsymbol{E}_b\} = [C_{bb}]\{\boldsymbol{F}_b\} + \{\boldsymbol{Z}_b\} \tag{2}$$

where the subscript b refers to discretization points on the imaging region boundary with n_b being the number of boundary points; $\{\boldsymbol{E}_b\}$ and $\{\boldsymbol{F}_b\}$ are the electric field and flux (i.e., $\boldsymbol{F} = \nabla E \cdot \hat{\boldsymbol{n}}$), respectively, at those points. $\{\boldsymbol{Z}_b\}$ is a column vector whose entries are $z_i = \langle fG_i \rangle$ for $i = 1$ to n_b where G_i is the unbounded-space Green's function (singular at node i) for the 2-D Helmholtz equation (in this case, the Hankel function) having an argument that is the product of the wavenumber (of the exterior region) times the distance from the nodes on the imaging boundary to the source location, and $\langle \cdot \rangle$ indicates integration over the problem domain. Matrices $[D_{bb}]$ and $[C_{bb}]$ are full and are described completely in [19] and [20]. Note that by eliminating the integration path around each discrete waveguide source, the size of these matrices is significantly reduced over those in [19] and [20] which has considerable impact on the computational costs since the inversion of matrix $[C_{bb}]$ is an $O(n_b^3)$ process. It also reduces the bandwidth of the full HE matrix problem since coupling of the full BE matrix to the sparse FE matrix has the net effect of increasing the resulting sparse matrix bandwidth in proportion to the size of the full BE matrix system.

The matrix formulation for the FE region remains the same as that derived in [19]

$$\begin{bmatrix} A_{II} & A_{Ib} \\ A_{bI} & A_{bb} \end{bmatrix} \begin{Bmatrix} \boldsymbol{E}_I \\ \boldsymbol{E}_b \end{Bmatrix} = \begin{bmatrix} 0 & 0 \\ 0 & B_{bb} \end{bmatrix} \begin{Bmatrix} 0 \\ \boldsymbol{F}_b \end{Bmatrix} \tag{3}$$

where the subscript I refers to nodes in the FE region that are not on the boundary (i.e., strictly interior). By solving (2) for $\{\boldsymbol{F}_b\}$ and substituting this into (3), we are left with

$$\begin{bmatrix} A_{II} & A_{Ib} \\ A_{bI} & A_{bb} - B_{bb}C_{bb}^{-1}D_{bb} \end{bmatrix} \begin{Bmatrix} \boldsymbol{E}_I \\ \boldsymbol{E}_b \end{Bmatrix} = \begin{bmatrix} 0 & 0 \\ 0 & -B_{bb}C_{bb}^{-1} \end{bmatrix} \begin{Bmatrix} 0 \\ \boldsymbol{Z}_b \end{Bmatrix} \tag{4}$$

which is used to compute the electric fields at all points within the FE mesh.

As described in [16], a matrix equation for computing the electric fields at designated points within the BE region was developed for the case of no source terms within that region. To utilize the same approach for the present case, the terms $\{\boldsymbol{Z}_x\}$ must be added to finally yield

$$\{\boldsymbol{E}_x\} = [Q_1]\{\boldsymbol{E}_b\} + [Q_2]\{\boldsymbol{F}_b\} + \{\boldsymbol{Z}_x\} \tag{5}$$

where $\{\boldsymbol{E}_x\}$ are the electric fields calculated at the set of points $\{X\} = (x_1, x_2, \cdots, x_{n_x})^T$ outside of the imaging region and $\{\boldsymbol{Z}_x\}$ contains the entries $z_i = \langle fG_i \rangle$ for $i = 1, 2, \cdots, n_x$, which are similar to those in $\{\boldsymbol{Z}_b\}$ except that the distance used in the argument of the Green's function is the distance from the source location to a point in $\{X\}$ instead of a point on the boundary, as is the case for $\{\boldsymbol{Z}_b\}$ (here n_x is the number of measurement sites within the BE region). Matrices $[Q_1]$ and $[Q_2]$ correspond to the terms associated with $(\partial G/\partial n)$ and G from the equation for calculating the electric field at a single point within the BE region

$$E_i = \oint \left(G_i \frac{\partial E}{\partial n} - \frac{\partial G_i}{\partial n} E \right) ds + \langle fG_i \rangle. \tag{6}$$

Modifications to the Jacobian matrix required for calculating the iterative material property updates manifest themselves in forms similar to the changes made to the forward problem solution. The first change is in the computation of $\{\partial \boldsymbol{E}_b / \partial k_i^2\}$ and $\{\partial \boldsymbol{F}_b / \partial k_i^2\}$ where k_i^2 is the value of k^2 (the wavenumber squared) at node i within the reconstruction mesh, which discretizes the electrical property distribution within the imaging region. This is accomplished by first taking the derivatives

with respect to k_i^2 of (2) and (3) to yield

$$\begin{bmatrix} \dfrac{\partial A_{II}}{\partial k_i^2} & \dfrac{\partial A_{Ib}}{\partial k_i^2} \\ \dfrac{\partial A_{bI}}{\partial k_i^2} & \dfrac{\partial A_{bb}}{\partial k_i^2} \end{bmatrix} \begin{Bmatrix} \boldsymbol{E}_I \\ \boldsymbol{E}_b \end{Bmatrix} + \begin{bmatrix} A_{II} & A_{Ib} \\ A_{bI} & A_{bb} \end{bmatrix} \begin{Bmatrix} \dfrac{\partial \boldsymbol{E}_I}{\partial k_i^2} \\ \dfrac{\partial \boldsymbol{E}_b}{\partial k_i^2} \end{Bmatrix} = \begin{bmatrix} 0 & 0 \\ 0 & B_{bb} \end{bmatrix} \begin{Bmatrix} 0 \\ \dfrac{\partial \boldsymbol{F}_b}{\partial k_i^2} \end{Bmatrix} \quad (7)$$

and

$$[D_{bb}] \left\{ \frac{\partial \boldsymbol{E}_b}{\partial k_i^2} \right\} = [C_{bb}] \left\{ \frac{\partial \boldsymbol{F}_b}{\partial k_i^2} \right\} \quad (8)$$

noting that the matrices $[B_{bb}]$, $[C_{bb}]$, $[D_{bb}]$, and the vector $\{\boldsymbol{Z}_b\}$ are not functions of k_i^2 and, hence, their derivatives are zero. Combining (7) and (8) yields

$$\begin{bmatrix} A_{II} & A_{Ib} \\ A_{bI} & A_{bb} - B_{bb} C_{bb}^{-1} D_{bb} \end{bmatrix} \begin{Bmatrix} \dfrac{\partial \boldsymbol{E}_I}{\partial k_i^2} \\ \dfrac{\partial \boldsymbol{E}_b}{\partial k_i^2} \end{Bmatrix} = - \begin{bmatrix} \dfrac{\partial A_{II}}{\partial k_i^2} & \dfrac{\partial A_{Ib}}{\partial k_i^2} \\ \dfrac{\partial A_{bI}}{\partial k_i^2} & \dfrac{\partial A_{bb}}{\partial k_i^2} \end{bmatrix} \begin{Bmatrix} \boldsymbol{E}_I \\ \boldsymbol{E}_b \end{Bmatrix}. \quad (9)$$

Calculation of $\{\boldsymbol{E}_I\}$ and $\{\boldsymbol{E}_b\}$ is already performed as part of the forward solution at each iteration. The entry-by-entry form of the matrix on the right-hand side of (9) is given in [9] and is not repeated here. The matrix on the left-hand side is exactly the same as that in the forward solution (4). Thus, calculation of $\{\partial \boldsymbol{E}_I / \partial k_i^2\}$ and $\{\partial \boldsymbol{E}_b / \partial k_i^2\}$ is relatively straightforward.

Since the present configuration utilizes measurement sites outside of the FE region, in particular at points $\{X\}$ within the BE region, calculation of $\{\partial \boldsymbol{E}_x / \partial k_i^2\}$ is also required. This is accomplished by first taking the derivative of (5):

$$\left\{ \frac{\partial \boldsymbol{E}_x}{\partial k_i^2} \right\} = [Q_1] \left\{ \frac{\partial \boldsymbol{E}_b}{\partial k_i^2} \right\} + [Q_2] \left\{ \frac{\partial \boldsymbol{F}_b}{\partial k_i^2} \right\} \quad (10)$$

noting that the matrices $[Q_1]$ and $[Q_2]$ and the vector $\{\boldsymbol{Z}_x\}$ do not vary with k_i^2 and, hence, their derivatives are also zero. Here, $[Q_1], [Q_2], \{\partial \boldsymbol{E}_b / \partial k_i^2\}$ and $\{\partial \boldsymbol{F}_b / \partial k_i^2\}$ have already been constructed via the previous computations, therefore, calculation of $\{\partial \boldsymbol{E}_x / \partial k_i^2\}$ requires two matrix–vector multiplications which do not significantly impact the overall computational costs.

B. New Calibration Procedure

The existing calibration procedure [13] which transforms field-measurement data from a three-dimensional (3-D) to a two-dimensional (2-D) representation makes assumptions at two key steps. First, in computing the magnitude and phase offsets, a certain amount of measurement data is taken at selected locations in a homogeneous medium from which the procedure calculates the phase center of the waveguide radiator and the electrical properties of the medium using a least-squares approach. From this information the 3-D and 2-D loss factors are calculated, which are subtracted out of and reintroduced into the measurement data, respectively. The approach requires a high level of antenna-position accuracy and ignores any magnitude and phase changes that may result from the bending of cables and the engaging and disengaging of coaxial connectors (during manual repositioning of the radiator and receiver elements). Second, when the actual raw measurement data is being collected for use in the reconstruction algorithm, the same assumptions are made about the antenna position accuracy and the magnitude and phase contributions from cable bending and connector engaging and disengaging. These potentially contribute errors to each individual measurement. In this section, we introduce a new four-step calibration procedure which improves the match of the measurement data to that computed, which subsequently improves the general image quality obtained.

Step 1: Calculation of the Electrical Properties of the Homogeneous Background Medium

This can be accomplished by one of two techniques: using the first step in the existing least squares calibration procedure or using an HP85070B dielectric probe kit in conjunction with the HP 8753C Network Analyzer. As a good check, the results of these two techniques have been compared to ensure the measurement accuracy.

Step 2: Calculation of the Electric Fields at the Measurement Sites

Given the electrical properties of the homogeneous medium from *Step 1*, the calculated electric fields $\{E^c_{\text{homogeneous}}\}$ can be computed (using the algorithm described in the previous section) at the required measurement sites. Since this algorithm employs a 2-D model, the calculated values will already include the desired 2-D free-space loss factor.

Step 3: Measurement of the Electric Fields with and without the Test Phantom Present

With the antennas, cables, and connector positions fixed for each transmit and receive antenna permutation, the electric fields measured for a homogeneous target region $\{\boldsymbol{E}^m_{\text{homogeneous data}}\}$ and the electric fields measured in the presence of the test phantom $\{\boldsymbol{E}^m_{\text{phantom test data}}\}$ are recorded. It is important to note that both of these measurement sets include multiplicative terms with: 1) the same 3-D free space loss factors; (2) the same magnitude and phase errors due to the antenna position inaccuracies; and 3) the same magnitude and phase errors due to cable bends and variations from engaging and disengaging of the connectors. Taking the logarithm and forming the difference of these two quantities

$$\log \left[\{E^m_{\text{phantom test data}}\} \right] - \log \left[\{E^m_{\text{homogeneous data}}\} \right] \quad (11)$$

yields a measured electric-field perturbation term which includes only the field variations due to the presence of the test

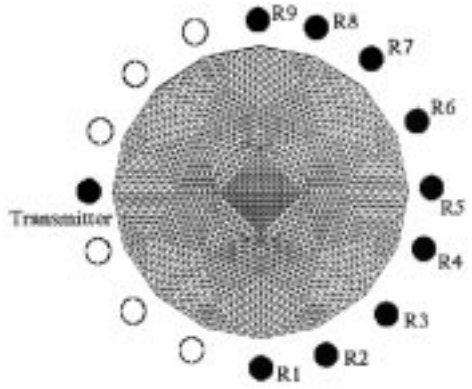

(a)

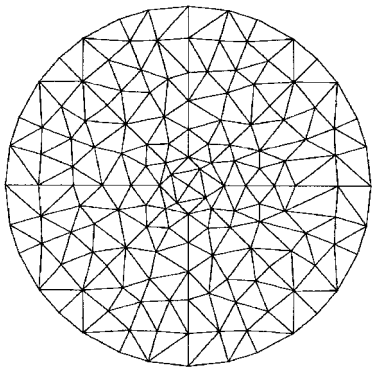

(b)

Fig. 1. FE meshes used for the monopole-based image reconstructions. (a) Field calculation mesh including radiate and receive antenna locations. (b) Property distribution mesh.

phantom with all of the other contributions—the free-space loss factor and various magnitude and phase errors—assumed to be canceled.

Step 4: Addition of the Resultant Terms from Steps 2 and 3

Taking the sum of the resultant terms from *Steps 2* and *3* will yield the logarithm of the calibrated electric-field measurements in the presence of the test phantom

$$\log\left[\{E^m_{\text{calibrated}}\}\right] = \log\left[\{E^c_{\text{homogenous}}\}\right] + \log[\{E^m_{\text{phantom test data}}\}] - \log\left[\{E^m_{\text{homogeneous data}}\}\right] \quad (12)$$

which can be transformed to produce $\{\boldsymbol{E}^m_{\text{calibrated}}\}$. Here, $\{\boldsymbol{E}^c_{\text{homogenous}}\}$ (and its logarithm) already contains the desired 2-D free-space loss factor. In essence, this technique combines the exact forward solution in the homogeneous medium having the correct free-space loss factor with the measurement electric-field offsets due to the introduction of the test phantom into the homogeneous medium while canceling the unwanted 3-D free-space loss factor along with the other unwanted magnitude and phase errors. This technique is most effective in a lossy medium which promotes minimization of the magnitude and phase errors due to mutual coupling of neighboring antennas, and for systems where the test phantoms are sufficiently far away from the antennas such that the radiation characteristics of the antennas themselves remain unperturbed.

TABLE I
ELECTRICAL PROPERTIES AT 700 MHz FOR THE MATERIALS USED IN THE IMAGING EXPERIMENTS

Material	Re(k^2) (ε_r)	Im(k^2) (σ - s/m)
Saline	16670 (77.44)	12150 (2.198)
Fat/Bone Equivalent	1198 (5.57)	103.4 (0.0187)
Agar (0.3% NaCl)	15310 (71.11)	5485 (0.9923)
Plexiglas	514.4 (2.39)	51.46 (0.00931)

III. RESULTS AND DISCUSSION

The monopole-transmitted measurement data was collected using the same prototype data-acquisition system described in [13] and [16] except for the type of transmitting antenna which has been selected. Full data sets were collected by manually moving the antennas to the prescribed positions (16 equally spaced locations on a 15-cm diameter circle surrounding the 14-cm diameter imaging region). Each of the 16 positions are used sequentially as the transmitting antenna location. With each active transmitting antenna, nine sites on the opposite side of the imaging region were used as the receiver locations. This technique provides a total of 144 measurement points for each image reconstruction. The mesh used for the forward solution computation is shown in Fig. 1(a) and illustrates the transmitter/receiver configuration for a sample transmitting location. The material property distribution was recovered on the more coarse mesh of Fig. 1(b) via the dual mesh scheme described in [18]. The electrical properties of the saline background and phantom objects which have been imaged are given in Table I. All data collection and concomitant image reconstruction were conducted at 700 MHz.

In the following subsections, we first demonstrate the improvements afforded by the new calibration procedure in the data–model match for both the monopole and waveguide systems. We also show that under equivalent calibrations, the data–model match for the monopole transmitters is superior to its waveguide counterparts. This improvement in data–model match is fundamental to achieving better image reconstructions with the near-field approach because the image reconstruction process is reliant on computational solutions which mimic the physical hardware system. Next, we compare reconstructed image accuracies obtained with the monopole and waveguide radiators based upon the new calibration approach in single-target experiments. We conclude by showing results from more complex multitarget imaging problems where we compare both new and old calibration procedures and waveguide and monopole image quality. These studies not only provide a vehicle for demonstrating that calibration-related image-reconstruction improvements occur under these more complicated conditions, but also a means of illustrating the general performance of our prototype monopole scheme *vis-à-vis* its waveguide counterpart.

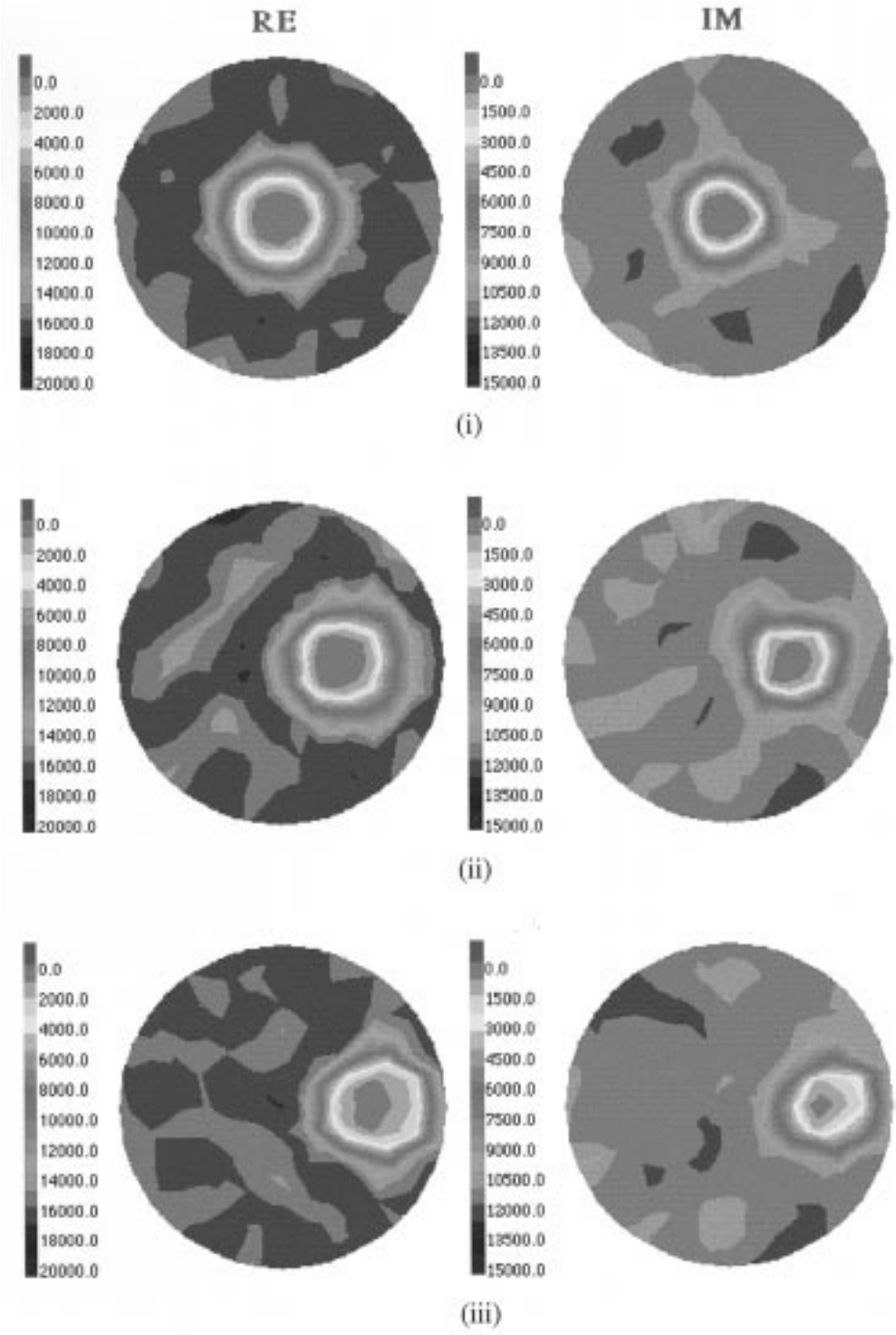

(a)

Fig. 2. (a) Reconstructed images of the complex k^2 distributions for a 4.3-cm-diameter bone/fat equivalent cylinder in a saline background for three locations using the monopole system with the new calibration procedure. (i) Centered. (ii) 2.5 cm to the right of center. (iii) 3.8 cm to the right of center.

A. Calibrated Measured Data Comparisons

The ability to exploit our iterative computational algorithm for image reconstruction is based upon the assumption that a good match exists between the calibrated measured data and the numerically calculated data in the presence of equivalent electrical property distributions. As we show in experiments reported in this section, both the new calibration procedure and the use of a monopole radiator (relative to waveguides) contribute to improvements in the underlying match between measured and computed data which translate into improved image quality, as demonstrated in the following subsections.

Experiments performed in [13] compared calibrated measured and computed data for a homogeneous target region

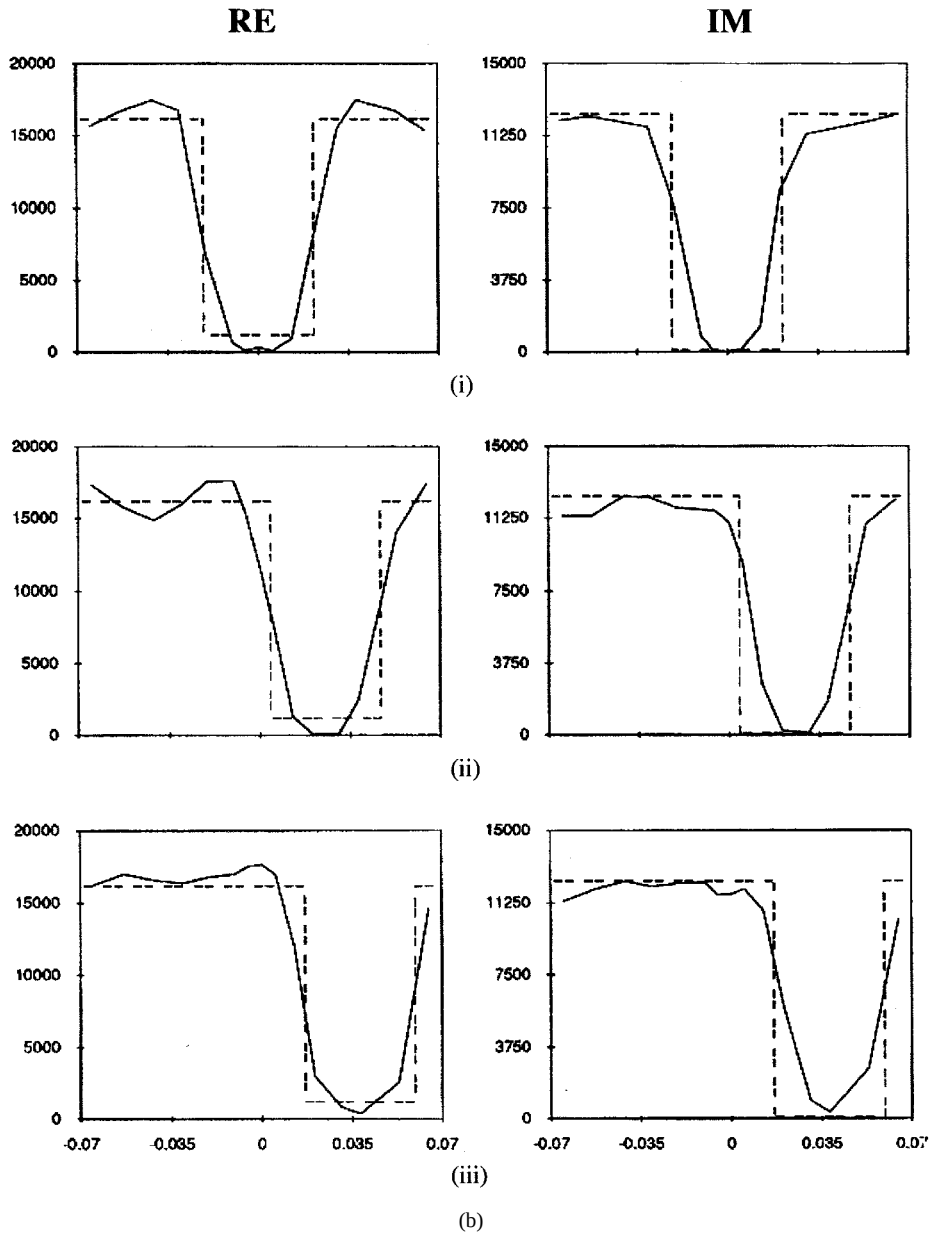

Fig. 2. *(Continued.)* (b) Longitudinal transects through the images shown in Fig. 2(a) displaying the reconstructed property profiles (solid lines) compared to the exact electrical property distributions (dashed lines).

under waveguide illumination. A more extensive study of data–model match has been undertaken here. Specifically, three different phantom configurations have been used to represent a variety of inhomogeneities within the target region:

1) single 4.3-cm-diameter bone/fat equivalent cylinder centered in the imaging region;
2) single 2.5-cm-diameter bone/fat equivalent cylinder offset 2.5 cm from the imaging region center;
3) 4.3- and 2.5-cm-diameter bone/fat equivalent cylinders separated by 1.7 cm.

Four combinations of radiator and calibration procedure have been examined:

1) waveguide radiator using the old calibration procedure;
2) waveguide radiator using the new calibration technique;
3) monopole radiator using the old calibration procedure;
4) monopole radiator using the new calibration technique.

For each target problem, 144 electric-field measurements were subtracted from the numerically calculated field values at the measurement site locations. These differences were then averaged. The results are shown in Table II(a) for the monopole radiator and Table II(b) for the waveguide radiator. It is clear that for all target configurations studied there is consistent improvement with calibration procedure independent of radiator used, and with the monopoles (relative to waveguides) independent of the calibration technique employed, leaving the new calibration/monopole radiator combination as providing the best data–model match. In particular, the field magnitude and phase match of the combined monopole radiator/new

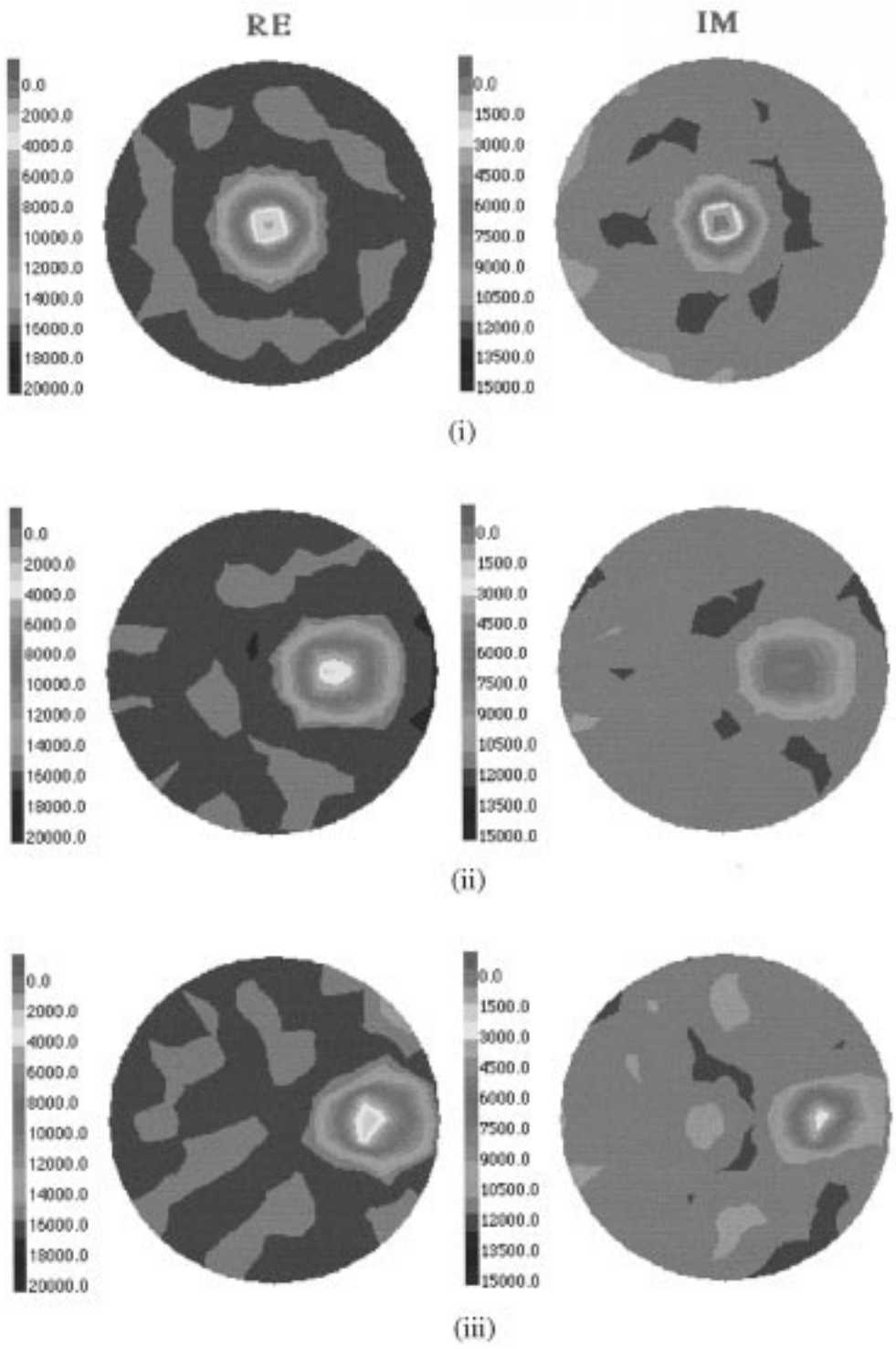

(a)

Fig. 3. (a) Reconstructed images of the complex k^2 distributions for a 2.5 cm diameter bone/fat equivalent cylinder in a saline background for three locations using the monopole system with the new calibration procedure. (i) Centered. (ii) 2.5 cm to the right of center. (iii) 3.8 cm to the right of center.

calibration technique versus the waveguide radiator/old calibration technique has been improved by 0.9 dB and 15° on the average.

It is important to recognize that these improvements occur on a per-measurement basis and the entire foundation of near-field imaging rests on its ability to synthesize small changes in a large number of measurement observations; hence, incremental improvements in the forward solution model-to-measurement-data match become important. In the next two subsections, complete image reconstruction as well as quantitative analysis of the images is presented. The image reconstruction results are found to be consistent with the

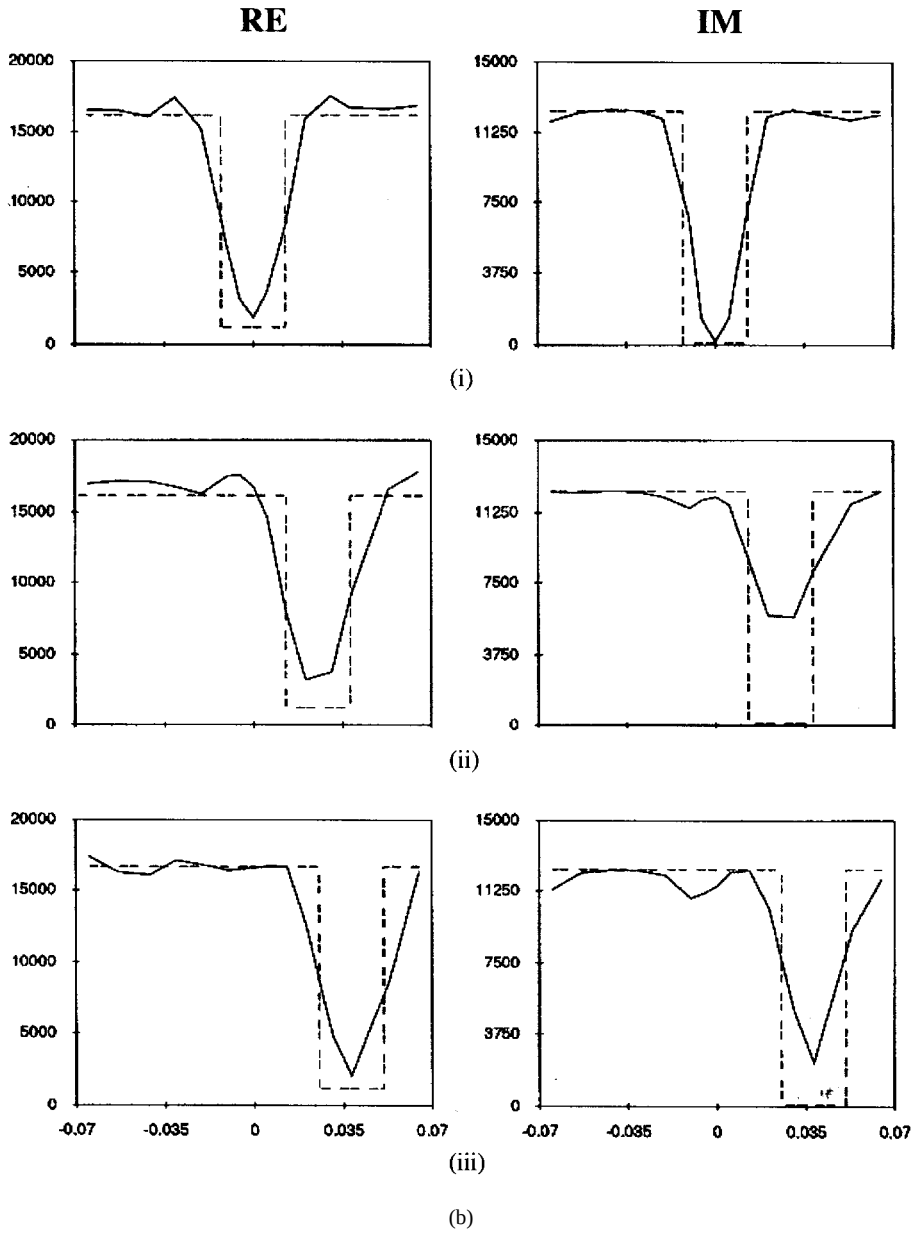

Fig. 3. *(Continued.)* (b) Longitudinal transects through the images shown in Fig. 3(a) displaying the reconstructed property profiles (solid lines) compared to the exact electrical property distributions (dashed lines).

data reported in Table II indicating that the degree to which data–model match can be realized is a critical factor in determining the final image quality.

B. Single-Target Imaging

Fig. 2(a) shows monopole images recovered at 700 MHz for a single 4.3–cm-diameter fat/bone equivalent cylinder at three locations:

1) centered;
2) offset 2.5 cm to the right of center;
3) offset 3.8 cm to the right of center.

Fig. 2(b) shows longitudinal transects through these images compared to the exact material property distribution to illustrate the level of quantitative agreement. Similarly, Fig. 3(a) contains monopole images reconstructed for a single 2.5-cm-diameter bone/fat equivalent cylinder at the same set of locations as in Fig. 2(a), with Fig. 3(b) displaying the corresponding longitudinal transects. In all of the above cases, the recovery of the object locations, shapes, and sizes agrees quite well with the exact material distributions. A corresponding set of image reconstructions have been obtained for the waveguide system using the new calibration procedures (not shown), and in order to compare these to the monopole cases we define a high-contrast image error as

$$\text{Image Error} = \sqrt{\frac{1}{L}\sum_{i=1}^{L}\left\langle \frac{(\chi_{\text{reconstruct}} - \chi_{\text{exact}})^2}{(\chi_{\text{background}} - \chi_{\text{exact}})^2}\right\rangle_i} \tag{13}$$

where χ represents the target property under evaluation (either real or imaginary component of k^2) and $\langle - \rangle_i$ indicates inte-

TABLE II
AVERAGE MAGNITUDE AND PHASE DIFFERENCES BETWEEN THE CALIBRATED MEASURED DATA AND THE CALCUALTED DATA FOR THREE DIFFERENT PHANTOMS FOR BOTH THE NEW AND OLD CALIBRATION PROCEDURES

Phantom	Old Calibration Procedure		New Calibration Procedure	
	Magnitude (dB)	Phase (deg.)	Magnitude (dB)	Phase (deg.)
4.3 cm diameter bone/fat equivalent cylinder centered in target region	1.754	9.379	1.442	5.308
2.5 cm bone/fat equivalent cylinder offset 2.5 cm to right of target region center	0.803	7.914	0.298	1.273
4.3 cm diameter and 2.5 cm diameter bone/fat equivalent cylinders separated by 1.7 cm.	1.323	9.484	1.304	5.419
Average	1.293	8.926	0.925	4.000

(a)

Phantom	Old Calibration Procedure		New Calibration Procedure	
	Magnitude (dB)	Phase (deg.)	Magnitude (dB)	Phase (deg.)
4.3 cm diameter bone/fat equivalent cylinder centered in target region	2.299	21.578	1.560	14.050
2.5 cm bone/fat equivalent cylinder offset 2.5 cm to right of target region center	1.244	11.076	0.545	3.120
4.3 cm diameter and 2.5 cm diameter bone/fat equivalent cylinders separated by 1.7 cm.	1.963	24.474	1.468	17.057
Average	1.835	19.043	1.191	11.409

(b)

TABLE III
IMAGE RECONSTRUCTION ERRORS FOR THE MONOPOLE AND WAVEGUIDE SYSTEMS IN THE 4.3-CM SINGLE-TARGET EXPERIMENT

	Target centered		Target 2.5 cm from center		Target 3.8 cm from center	
	Real	Imag	Real	Imag	Real	Imag
Monopole New cal.	0.1782	0.3177	0.1964	0.3231	0.1774	0.3434
Waveguide New cal.	0.2757	0.4123	0.2650	0.4368	0.2593	0.4563
Waveguide Old cal.	0.2864	0.7457	0.2674	0.4659	0.4327	1.2184

gration over the ith elemental area (of a total of L elements) comprising the target region. Table III reports this measure for the 4.3-cm-diameter target positioned at three spatial locations for the monopole and waveguide radiators, respectively. The data in the table reveals that the target recovery for the real and imaginary components of the electrical property distribution is improved by both the calibration procedure and the monopole radiators in all three cases.

Although not comprehensive, these comparisons indicate that the monopole system leads to an improvement in image reconstruction over the prototype waveguide approach under equivalent calibration procedures. As indicated by the results in Section III-A, this is likely due to the degree of data–model match which can be achieved for the monopole when a simple computational representation of the radiator is employed rather than due to some physical characteristics which favor the monopole relative to the waveguide source. When combined with the economy-of-space issues and the computational cost advantages of the monopoles over the waveguides, the evidence of enhanced accuracy in the reconstructed images (as demonstrated in Figs. 2, 3 and Table III) makes the monopole antennas an appealing choice as the radiator/receiver elements in near-field microwave imaging.

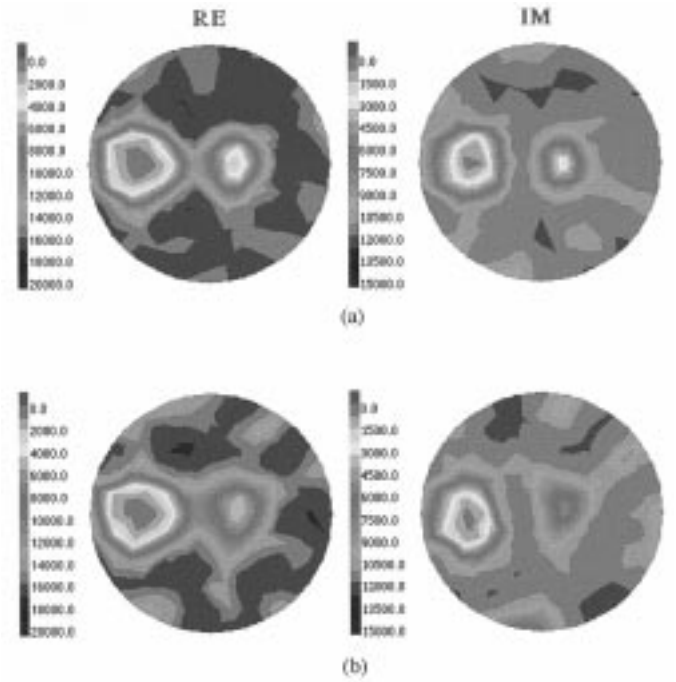

Fig. 4. Reconstructed images of the complex k^2 distributions for a 4.3-cm-diameter and a 2.5-cm-diameter bone/fat equivalent cylinder separated by 1.7 cm using the monopole system. (a) New calibration procedure. (b) Old calibration procedure.

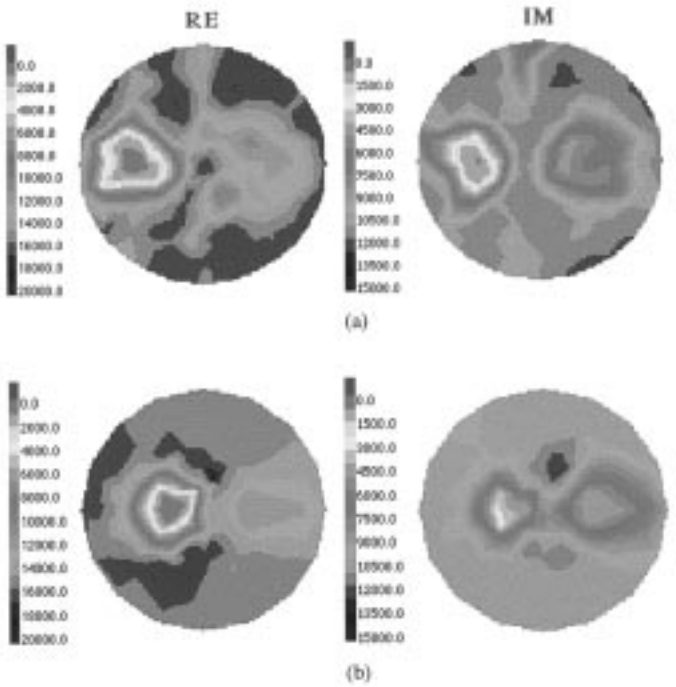

Fig. 5. Reconstructed images of the complex k^2 distributions using the new calibration procedure for a 4.3-cm-diameter bone/fat equivalent cylinder and a 3.8-cm-diameter (0.3-cm-thick wall) Plexiglas cylinder filled with an agar gel having 0.3% NaCl separated by 1.4 cm. (a) Monopole system. (b) Waveguide system.

C. Multitarget Imaging

In this section, monopole-imaging performance and its associated improvement afforded by the new calibration procedure is examined further through several multitarget imaging

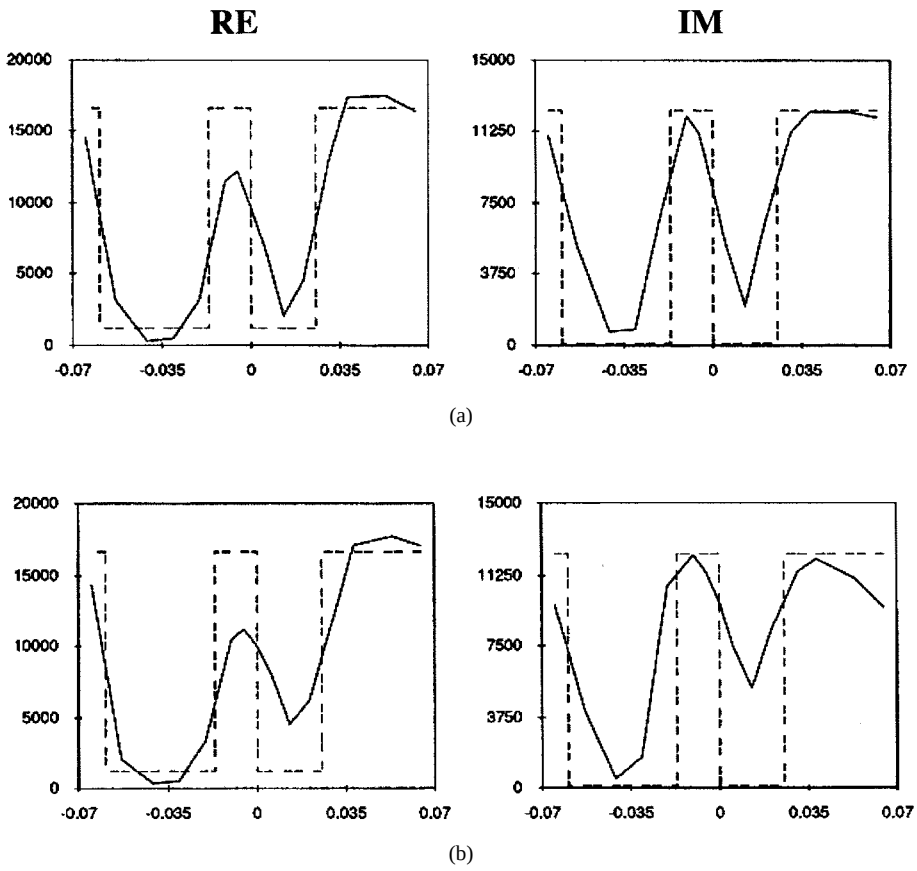

Fig. 6. Longitudinal transects displaying the reconstructed property profile (solid lines) through the images shown in Fig. 4. (a) New calibration procedure. (b) Old calibration procedure.

experiments. The first test case consists of two bone/fat equivalent cylinders (4.3- and 2.5-cm diameters, respectively) separated by 1.7 cm. Fig. 4 show the images reconstructed from measured data using both the new and old calibration procedures. The second test, which highlights the advantages of the monopole transmitter system over the waveguide transmitter system (under equivalent conditions), consists of images recovered from the 4.3-cm-diameter bone/fat cylinder separated by 1.7 cm from a 3.8-cm-diameter Plexiglas cylinder filled with an agar solution which contains 0.3% NaCl. The reconstructed images based upon the two transmitter types are shown in Fig. 5(a) and (b).

Longitudinal transects through the images presented in Fig. 4 are compared with the exact material property profile in Fig. 6. There are several observations to note which further support the contention that the improved data–model match afforded by the new calibration approach leads to enhanced image reconstruction. First, the shape of the objects for both the real and imaginary parts more closely resembles that of the true targets for the new calibration procedure. Second, the background and the material properties within the objects are more uniform using the new procedure. Third, the edges between two neighboring objects appear to be more discernible for the images using the new procedure, suggesting spatial resolution improvements. Finally, the imaginary part of the recovered object material properties is closer to the known values using the new procedure.

Fig. 7 contains the longitudinal transects corresponding to the images in Fig. 5 which compare monopole- and waveguide-imaging performance when the new calibration procedure is applied to both data-acquisition systems. An added degree of complexity for the image reconstruction problem in this case is the presence of the 0.3-cm-thick Plexiglas-cylinder wall. Looking at the material properties listed in Table I, one can observe that this thin wall has an electrical contrast with the surrounding medium of roughly $37:1$ in the real part and over $100:1$ in the imaginary part. The wall thickness makes it prohibitively difficult to recover the material properties of the plastic exactly; however, the general shape and location of the wall are discernible in the monopole system while less apparent in the waveguide case. It should be noted that the reconstructed ring is also more pronounced in the real part of the images due to the relatively lower contrast level of the plastic with both the materials inside and outside of the cylinder; while in the imaginary part, the faint detection of the shell is not observed because of the extremely high contrast level (three times greater than the real part). Table IV shows the image errors resulting from a quantitative analysis of these reconstructed images. In the case of agar, we define a low-contrast image error as

$$\text{Image Error} = \sqrt{\frac{1}{L}\sum_{i=1}^{L}\left\langle \frac{(\chi_{\text{reconstruct}} - \chi_{\text{exact}})^2}{(\chi_{\text{exact}})^2} \right\rangle_i} \tag{14}$$

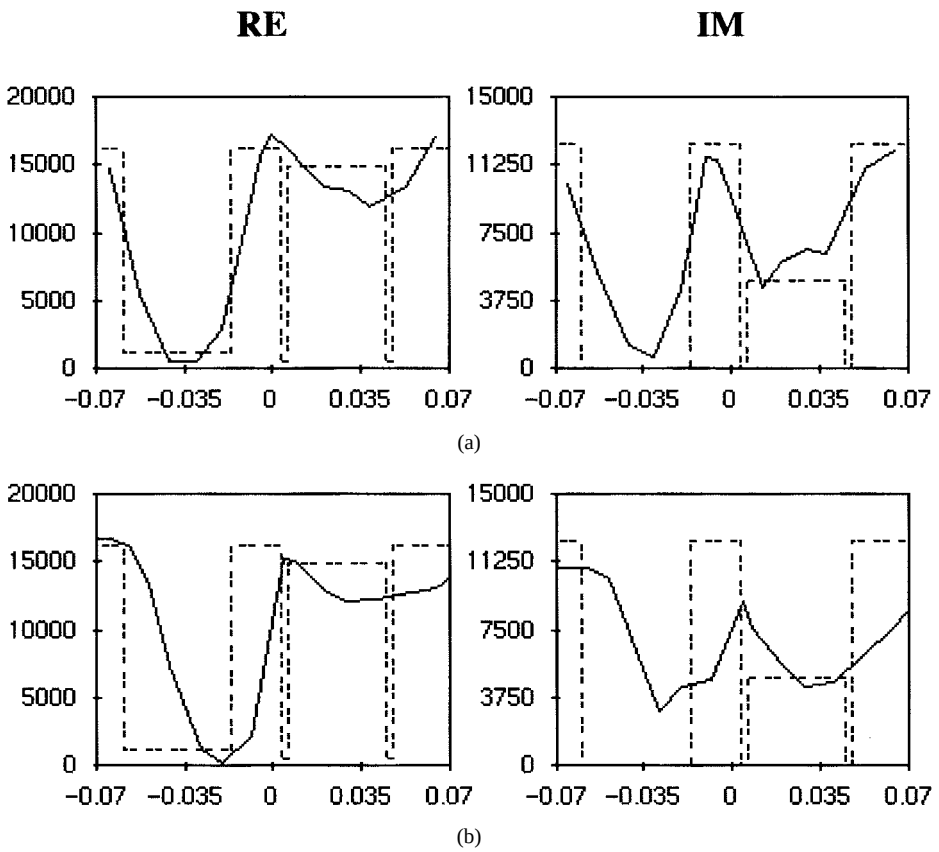

Fig. 7. Longitudinal transects displaying the reconstructed property profiles (solid lines) through the images shown in Fig. 5 compared to the exact electrical property distributions (dashed lines). (a) Monopole system. (b) Waveguide system.

which is similar to the high-contrast image error (used for the bone/fat target) of (13), except for the normalization.

The data in Table IV supports the notion that the monopoles outperform their waveguide counterparts for the most part, although perhaps not as consistently as in the single-target experiments. For both radiators, the presence of the Plexiglas ring serves to degrade the resulting image quality, but even in this demanding situation there does appear to be a small systematic and quantitatively measurable improvement with the monopoles in terms of identifying the ring.

The final set of images in this section report results for a three-target phantom experiment using the 2.5- and 4.3-cm-diameter bone/fat equivalent cylinders along with the 3.8-cm-diameter Plexiglas cylinder of agar. Because these objects are not placed along a common axis such that a useful exact-material property transect can be obtained (as in the previous imaging experiments), a color image of the exact-material property distribution is shown in Fig. 8(a) for comparison purposes. Note that these images also illustrate the thin ring of the Plexiglas cylinder. Fig. 8(b) and (c) show the images recovered for this experiment using the new and old calibration procedures, respectively. The observations are generally similar to those noted earlier—more uniform background, better object shape definition, and improved spatial resolution for the images which used the new calibration procedure. Again, the Plexiglas wall is readily visible, especially in the real part of the electrical property distribution, when the reconstructions are based on the new calibration [see Fig. 8(b)] compared to the old calibration technique. These multitarget experiments illustrate that this new monopole system and associated calibration procedure is viable in problems other than those involving simple single-target reconstructions.

TABLE IV
IMAGE RECONSTRUCTION ERRORS FOR THE MONOPOLE AND WAVEGUIDE SYSTEMS IN THE MULTITARGET PROBLEM CONSISTING OF ONE 4.3-CM-DIAMETER BONE/FAT TARGET AND ONE PLEXIGLAS ENCLOSED AGAR GEL TARGET USING THE NEW CALIBRATION PROCEDURE

	Bone/fat target		Agar target		Plexiglass target	
	Real	Imag	Real	Imag	Real	Imag
Monopole	0.2171	0.3347	0.1422*	0.1399	0.7821	0.5592
Waveguide	0.4542	0.5168	0.1204*	0.2192	0.8159	0.5776

All image error values are based upon the high contrast criteria of equation 13 unless otherwise indicated.

* Image error values are based upon the low contrast criteria of equation 14.

IV. SUMMARY AND CONCLUSIONS

In this paper, we have implemented a monopole transceiver near-field imaging system and have conducted a number of preliminary experiments in order to examine its imaging performance. The monopole implementation has required alterations within our previously reported image-reconstruction algorithm which was based upon waveguide illumination. In addition, a new calibration procedure has been recognized and applied to data collected from both monopole and waveguide radiators. A series of single and multitarget imaging

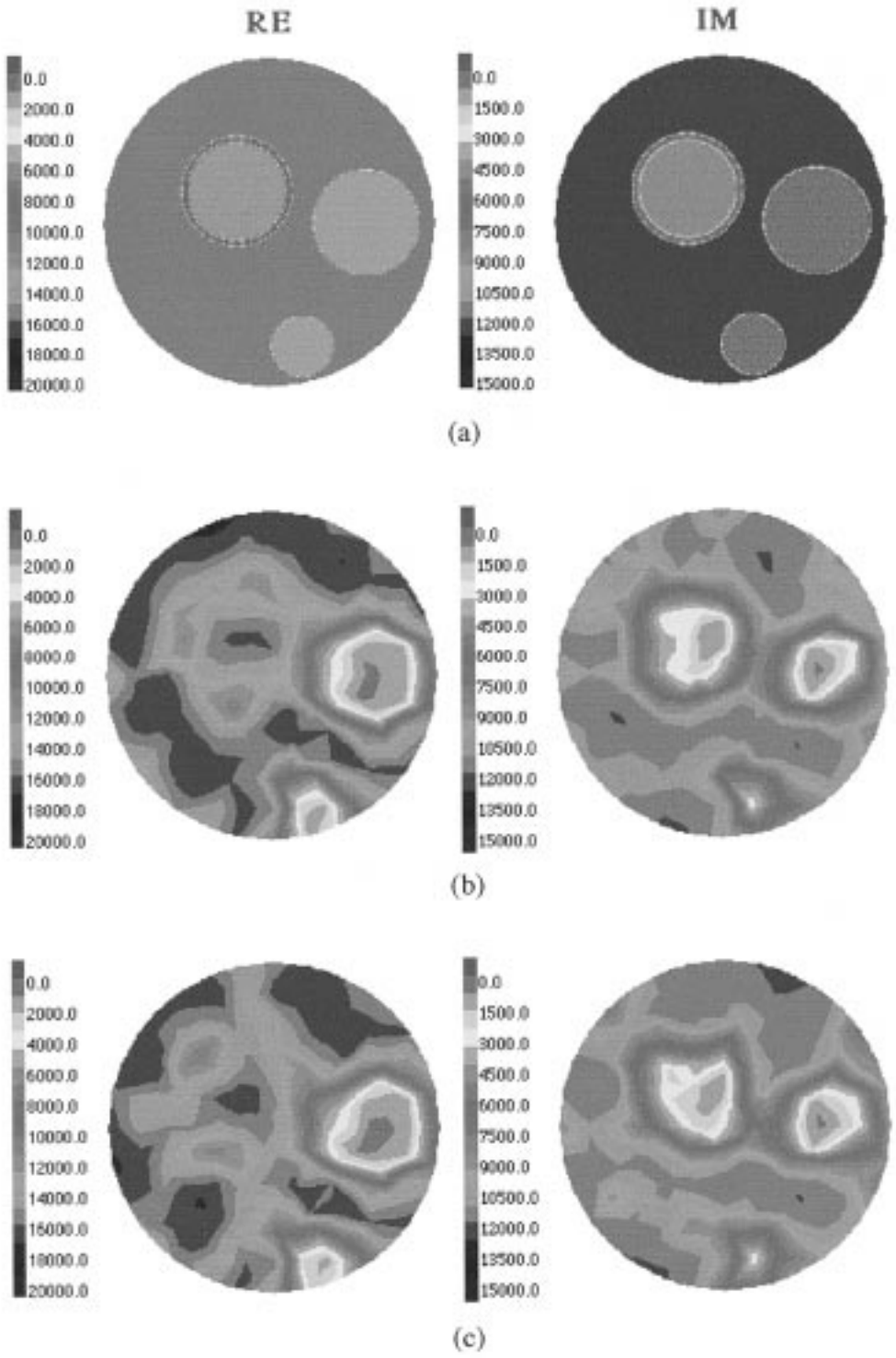

Fig. 8. Reconstructed images of the complex k^2 distributions achieved for a three-object phantom including in clockwise order from the upper left: (i) the 3.8-cm-diameter Plexiglas cylinder filled with a 0.3% NaCl agar gel, (ii) the 4.3-cm-diameter bone/fat equivalent cylinder, and (iii) the 2.5-cm-diameter bone/fat equivalent cylinder. (a) Exact property images. (b) New calibration procedure. (c) Old calibration procedure.

experiments have been used to illustrate the overall quality of the monopole reconstructions and the importance of the new calibration approach.

Technically, the incorporation of the monopole radiator is both physically and computationally straightforward. In fact, we have shown that the monopole radiator can be treated as a line-source term within our HE reconstruction algorithm at a considerably reduced computational cost relative to its waveguide counterpart. Primarily, a reduction in the hybrid FE/BE matrix system bandwidth is achieved, which results in a factor of four increase in forward solution speed assuming that an equal number of nodes are devoted to the waveguide

and imaging region boundary discretizations, respectively (i.e., the bandwidth is cut in half and the forward solution costs scale as the square of the bandwidth). This economy also translates into a factor-of-two increase in the Jacobian construction speed which scales linearly in the bandwidth. The ability to successfully incorporate either a waveguide or monopole radiator in the near-field imaging context adds further credibility to our previous claims about the flexibility of the HE approach as the basis for image reconstructions [9], [18].

The new calibration procedure which has been identified is independent of the type of radiator which is used—yet systematically improves image quality. The source of this improvement is the enhancement in the data–model match when simple computational representations of the transmitter are employed. The procedure serves to eliminate positioning and feed-cable errors while simultaneously replacing the intrinsic 3-D loss factor with an equivalent 2-D loss factor. Results show that magnitude differences are improved by 0.4 dB and phase discrepancies are improved by 5° (on average) on a per-measurement basis relative to our earlier scheme. These improvements clearly manifest themselves in the final reconstructed images. Specifically, more accurate object shape determination, more recovered-property uniformity within the background, better qualitative spatial resolution in discriminating edges in neighboring targets, and improved recovery in the imaginary component of the electrical properties of the embedded objects have all been consistently observed in both single and multitarget image reconstructions.

There is also evidence to suggest that the monopole radiators systematically result in better quality images than waveguide radiators within our prototype imaging-system approach. This finding is supported by a series of direct measurements obtained in three separate phantom configurations of increasing complexity where comparisons of computed results were made at each measurement site for all radiator positions. The data shows an improved match when the monopole system is used independent of the calibration procedure employed indicating that the simple radiator models we have used are better able to represent the monopole transmitter. Specifically, an approximate improvement of 0.3 dB in magnitude and 7° in phase has been realized in the data–model match with the monopole system and these improvements, though modest on a per measurement basis, do translate into enhanced image reconstruction. Under identical imaging conditions using the new calibration procedures for both types of radiators, the monopole image errors within the target region can be as much as 20% smaller than those occurring in the corresponding waveguide images, and these error reductions appear in both the real and imaginary components of the property distributions—although the biggest gains occur in the imaginary part. Particularly impressive is the ability to recover the presence of a thin-walled Plexiglas ring surrounding certain targets. Again, this performance improvement with the monopole is attributed to enhanced data–model match rather than some intrinsic physical characteristics of the monopole transmitter over its waveguide counterpart. While further experimentation may be warranted to definitely establish the superiority of the monopole system relative to the waveguides, and to define the range of these differences under representative conditions, there are other compelling reasons to use monopoles, including their economy-of-space advantages, their simplicity, low cost, and the ease with which they can be modeled. Thus, the fundamental importance of the monopole results contained herein is the demonstration that their resultant near-field images are certainly no worse (and likely better!) than their waveguide counterparts.

REFERENCES

[1] L. E. Larsen and J. H. Jacobi, *Medical Applications of Microwave Imaging*. Piscataway, NJ: IEEE Press, 1986.

[2] R. Maini, M. F. Iskander, C. H. Durney, and M. Berggren, "On the sensitivity and resolution of microwave imaging using ART," *Proc. IEEE*, vol. 69, pp. 1517–1519, Nov. 1981.

[3] R. Maini, M. F. Iskander, and C. H. Durney, "On electromagnetic imaging using linear reconstruction techniques," *Proc IEEE*, vol. 68, pp. 1550–1552, Dec. 1980.

[4] J. C. Bolomey, C. Pichot, G. Gaboriaud, "Planar microwave imaging camera for biomedical applications: Critical and prospective analysis of reconstruction algorithms," *Radio Sci.*, vol. 26, pp. 541–550, 1991.

[5] N. Jaochimowicz, C. Pichot, and R. Hugonin, "Inverse scattering: An iterative numerical method for electromagnetic imaging," *IEEE Trans. Antennas Propagat.*, vol. 39, pp. 1742–1752, Dec. 1991.

[6] S. Caorsi, G. L. Gragnani, and M. Pastorino, "A multi-view microwave imaging system for two dimensional penetrable objects," *IEEE Trans. Microwave Theory Tech.*, vol. 39, pp. 845–851, May 1991.

[7] ———, "Reconstruction of dielectric permittivity distributions in arbitrary 2-D inhomogeneous biological bodies by a multiview microwave numerical method," *IEEE Trans. Med. Imag.*, vol. 12, pp. 232–239, June 1993.

[8] S. Caorsi, S. Ciaramella, G. L. Gragnani, and M. Pastorino, "On the use of regularization techniques in numerical inverse scattering solutions for microwave imaging applications," *IEEE Trans. Microwave Theory Tech.*, vol. 43, pp. 632–640, Mar. 1995.

[9] P. M. Meaney, K. D. Paulsen, and T. P. Ryan, "Two-dimensional hybrid element image reconstruction for TM illumination," *IEEE Trans. Antennas Propagat.*, vol. 43, pp. 239–247, Mar. 1995.

[10] A. Franchois and C. Pichot, "Microwave imaging-complex permittivity reconstruction with a Levenberg–Marquardt Method," *IEEE Trans. Antennas Propogat.*, vol. 45, pp. 203–215, Feb. 1997.

[11] J. C. Bolomey, "Recent European developments in active microwave imaging for industrial, scientific and medical applications," *IEEE Trans. Microwave Theory Tech.*, vol. 37, pp. 2109–2117, Dec. 1989.

[12] L. Jofre, M. S. Hawley, A. Broquetas, E. de los Reyes, M. Ferrando, A. R. Elias-Fuste, "Medical imaging with a microwave tomographic scanner," *IEEE Trans. Biomed. Eng.*, vol. 37, pp. 303–312, Mar. 1990.

[13] P. M. Meaney, K. D. Paulsen, A. Hartov, and R. C. Crane, "An active microwave imaging system for reconstruction of 2-D electrical property distributions," *IEEE Trans. Biomed. Eng.*, vol. 42, pp. 1017–1026, Oct. 1995.

[14] S. Y. Semenov, R. H. Svenson, A. E. Boulyshev, A. E. Souvorov, V. Y. Borisov, Y. Sizov, A. N. Starostin, K. R. Dezern, T. P. Tatsis, and V. Y. Baranov, "Microwave tomography: Two dimensional system for biological imaging," *IEEE Trans. Biomed. Eng.*, vol. 43, pp. 869–877, Sept. 1996.

[15] J. C. Lin, "Frequency optimization for microwave imaging of biological tissues," *Proc. IEEE*, vol. 73, pp. 374–375, Feb. 1985.

[16] P. M. Meaney, K. D. Paulsen, A. Hartov, and R. C. Crane, "Microwave imaging for tissue assessment: Initial evaluation in multi-target tissue equivalent phantoms," *IEEE Trans. Biomed. Eng.*, vol. 43, pp. 878–890, Sept. 1996.

[17] P. M. Meaney, "Microwave imaging for 2-D electrical property distribution profiling," Ph.D. dissertation, Thayer School Eng., Dartmouth College, 1995.

[18] K. D. Paulsen, P. M. Meaney, M. J. Moskowitz, J. M. Sullivan, Jr., "A dual mesh scheme for finite element based reconstruction algorithms," *IEEE Trans. Med. Imag.*, vol. 14, pp. 504–514, Sept. 1995.

[19] K. D. Paulsen and W. Liu, "Memory and operations count scaling for coupled finite-element and boundary-element systems of equations," *Int. J. Numer. Methods Eng.*, vol. 33, pp. 1289–1304, 1992.

[20] D. R. Lynch, K. D. Paulsen, and J. W. Strohbehn, "Hybrid element method for unbounded electromagnetic problems in hyperthermia," *Int. J. Numer. Methods Eng.*, vol. 23, pp. 1915–1937, 1986.

Paul M. Meaney (S'91) received the A.B. degree in electrical engineering and computer science from Brown University, Providence, RI, in 1982, the M.S. degree in electrical engineering from the University of Massachusetts at Amherst, in 1985, and the Ph.D. degree in engineering from Dartmouth College, Hanover, NH, in 1995.

From 1985 to 1991, he worked for Millitech Corporation and Alpha Industries, designing millimeter-wave components and subsystems. He then became a Research Assistant at the Thayer School of Engineering, Dartmouth College, and subsequently worked as Post-Doctoral Fellow at both the Thayer School and the Royal Marsden Hospital, Sutton, U.K. He is currently a Research Assistant at the Thayer School. His current research interests include antenna theory and inverse-scattering problems, especially those related to the imaging of electrical property distributions in biological tissue and to ultrasound-based elasticity imaging.

Keith D. Paulsen (S'85–M'86) received the B.S. degree in biomedical engineering from Duke University, Durham, NC, in 1981 and the M.S. and Ph.D. degrees in engineering from Dartmouth College, Hanover, NH, in 1984 and 1986, respectively.

He is currently an Associate Professor at the Thayer School of Engineering, Dartmouth College, and is also with the Dartmouth–Hitchcock Medical Center, Lebanon, NH. His current research interests include numerical electromagnetics for application in biomedical problems and remote sensing.

John T. Chang received the B.S., M.S., and Ph.D. degrees in electrical engineering from Northwestern University, Evanston, Il, in 1988, 1989, and 1995, respectively.

He is currently a Post-Doctoral Research Associate at the Thayer School of Engineering, Dartmouth College, Hanover, NH. His current research interests include computational and experimental electromagnetics, inverse problems, remote sensing, and electromagnetic characterization of high technology and biologically-based materials.